Investigations on ion implantation-induced strain in rotated Y-cut LiNbO₃ and LiTaO₃

Zhongxu Li(李忠旭), Kai Huang(黄凯), Yanda Ji(吉彦达), Yang Chen(陈阳), Xiaomeng Zhao(赵晓蒙), Min Zhou(周民), Tiangui You(游天桂), Shibin Zhang(张师斌), and Xin Ou(欧欣)

What follows is a list of articles you may be interested in

Hydrogen isotopic replacement and microstructure evolution in zirconium deuteride implanted by 150 keV protons

Man Zhao(赵嫚), Mingxu Zhang(张明旭), Tao Wang(王韬), Jiangtao Zhao(赵江涛), Pan Dong(董攀), Zhen Yang(杨振), and Tieshan Wang(王铁山)

Structural, magnetic, and dielectric properties of Ni-Zn ferrite and Bi₂O₃ nanocomposites prepared by the sol-gel method

Jinmiao Han(韩晋苗), Li Sun(孙礼), Ensi Cao(曹恩思), Wentao Hao(郝文涛), Yongjia Zhang(张雍家), and Lin Ju(鞠林)

Anti-oxidation characteristics of Cr-coating on surface of Ti-45Al-8.5Nb alloy by plasma surface metallurgy technique

Bing Zhou(周兵), Ya-Rong Wang(王亚榕), Ke Zheng(郑可), Yong Ma(马永), Yong-Sheng Wang(王永胜), Sheng-Wang Yu(于盛旺), and Yu-Cheng Wu(吴玉程)

Microwave-assisted synthesis of Mg:PbI₂ nanostructures and their structural, morphological, optical, dielectric and electrical properties for optoelectronic technology

Mohd. Shkir, Ziaul Raza Khan, T Alshahrani, Kamlesh V. Chandekar, M Aslam Manthrammel, Ashwani Kumar, and S AlFaify$

Isostructural phase transition-induced bulk modulus multiplication in dopant-stabilized ZrO₂ solid solution

Min Wang(王敏), Wen-Shu Shen(沈文舒), Xiao-Dong Li(李晓东), Yan-Chun Li(李延春), Guo-Zhao Zhang(张国召), Cai-Long Liu(刘才龙), Lin Zhao(赵琳), Shu-Peng Lv(吕舒鹏), Chun-Xiao Gao(高春晓), Yong-Hao Han(韩永昊)

Investigations on ion implantation-induced strain in rotated Y-cut LiNbO₃ and LiTaO₃*

Zhongxu Li(李忠旭),[1,3,†], Kai Huang(黄凯)[1,4,†], Yanda Ji(吉彦达)[2], Yang Chen(陈阳),[1,3], Xiaomeng Zhao(赵晓蒙)[1,4], Min Zhou(周民)[1], Tiangui You(游天桂)[1], Shibin Zhang(张师斌)[1], and Xin Ou(欧欣)[1,3,‡]

[1] State Key Laboratory of Functional Materials for Informatics, Shanghai Institute of Microsystem and Information Technology, Chinese Academy of Sciences (CAS), Shanghai 200050, China
[2] MIIT Key Laboratory of Aerospace Information Materials and Physics & College of Science, Nanjing University of Aeronautics and Astronautics, Nanjing 211106, China
[3] Center of Materials Science and Optoelectronics Engineering, University of Chinese Academy of Sciences, Beijing 100049, China
[4] Shanghai Novel Silicon Integration Technology Co., Ltd., Jiading, Shanghai, China

The monocrystalline LiNbO₃ (LN) and LiTaO₃ (LT) plates have been qualified as a kind of material platform for high performance RF filter that is considerable for the 5G communication. LN and LT thin films are usually transferred on handle wafers by combining ion-slicing and wafer bonding technique to form a piezoelectric on insulator (POI) substrate. The ion implantation is a key process and the implantation-induced strain is essential for the layer transfer. Here, we reported the strain profile of ion implanted rotated Y-cut LN and LT. The ion implantation generates the out-of-plane tensile strain of the sample surface and (006) plane, while both the tensile and compressive strain are observed on the (030) plane. The implanted ions redistributed due to the anisotropy of LN and LT, and induce the main tensile normal to the (006) plane. Meanwhile, the (030) planes are contracted due to the Poisson effect with the interstitial ions disturbing and mainly show a compressive strain profile.

1. Introduction

With the momentous demand of mobile communication, the new generation of mobile network is introduced approximately every ten years. The fifth-generation (5G) network provides high data rate and extended capacity via accessing higher frequency bands and larger physical bandwidths.[1–6] Compared with 4G LTE, sub-6 GHz 5G network requires improved filter performances such as high frequency, large fractional bandwidth (FBW), low insertion loss, high out-of-band rejection, and excellent temperature stability. However, the low central frequency of the surface acoustic wave (SAW) resonator and the insufficient FBW of the film bulk acoustic resonator (FBAR) are the main challenges of the acoustic wave filters.[7] In recent years, the characteristics of acoustic wave propagating in piezoelectric single-crystalline plate have been attracting attention.[8–11] Micro actuators with a record-high figure of merit were realized on the (YXl)36° cut LiNbO₃ (LN) thin plate,[12] and the incredible-high-performance SAW (IHP SAW) filters with high Q factor and minimal TCF have been fabricated on (YXl)42° cut LiTaO₃ (LT) thin film.[8]

Due to the high anisotropy of LN and LT, the large propagation velocity and high electromechanical coupling coefficients k^2 are achieved in special orientations, *i.e.*, functional cuts.[5,6,13,14] The ion-slicing technique, combining the crystal-ion-slicing (CIS) and heterogeneous wafer bonding, is one of the mainstream methods of fabricating thin LN/LT plates with versatile orientations.[8–11,15] Ion implantation introduces microscopic defects and strains,[16,17] and the strain profile have a significant influence on the defect evolution and CIS, although it will be disappeared trough a high temperature anneal.[18] The defects and strains of ion-implanted LN were widely investigated by the x-ray diffraction (XRD), but the strain profile in rotated Y-cut LN and LT was less investivated.[19–21] Hence, it remains a lack of the detailed information of desired crystallographic planes changes to investigate the detail information of CIS.

In this work, the strain profiles in ion-implanted (YXl)36° cut LN and (YXl)42° cut LT were investigated. The out-of-

---

†These authors contributed equally to this work.
‡Corresponding author. E-mail: ouxin@mail.sim.ac.cn

plane strain of the (012), (006), and (030) planes were measured through the high resolution x-ray diffraction (HRXRD), and the reciprocal space maps were plotted. A compressive strain exhibited in (030) plane among all the implanted rotated cut LN and LT samples, which is attributed to the large tensile strain in the z direction of crystal structure ((006) plane) after ion implantation.

2. Experimental details

In the present study, the (YXl)36° cut LN was implanted by 160-keV He ions and the (YXl)42° cut LT was implanted by 75-keV H ions.[8,18,22] Both the ion species and the ion fluence are based on the conditions for CIS of LN and LT. The ion implantation was conducted at room temperature and the samples were tilted 7° from normal to minimize the channeling effect. The damage profile was calculated using the Stopping and Range of Ion Matter (SRIM 2008).[23] According to the SRIM simulation, the depth of the damage peak is about 530 nm for LN and 570 nm for LT, respectively. The coupled ω–2θ measurements were performed on the (012), (006), and (030) planes to investigate the strain profile using the Philips X'pert x-ray diffractometer. The symmetric and asymmetric RSM scans of (YXl)36° cut LN were conducted to further investigate the strain state.

3. Results and discussion

Owing to the strong anisotropy of single-crystalline LN and LT, SAW devices are fabricated on wafers with particular cut.[24,25] The orientation of the cut is specified by a series of rotations defined by the IEEE standard on piezoelectricity. As shown in Fig. 1(a), the x, y, z and x', y', z' represent the coordinate systems of the crystal and the substrate, respectively. The z' axis of the substrate is rotated 54° counter clockwise around the x (x') axis for the (YXl)36° LN, and the z' axis of the substrate is rotated counter clockwise around the x (x') axis 48° for the (YXl) 42° LT. Therefore, the angle between the wafer surface and the z axis of the crystal is 36° for the (YXl)36° cut LN and 42° for the (YXl)42° cut LT, respectively. LN and LT exhibit a similar crystal structure that can be described with a rhombohedral or a (three times larger) hexagonal unit cell containing 30 atoms.[26–28] The hexagonal unit cell of LN is shown in Fig. 1(b). From the crystallographic structure point of view, the angle between (012) plane and [001] is 36.6° (as the crystal unit cell parameters for LN are $a = b = 0.515$ nm and $c = 1.386$ nm)[28] for the (YXl)36 LN. Therefore, the (012) plane can be regarded to be quasi-parallel with the surface of (YXl)36° LN wafer.

For the rotated Y-cut LN and LT with angle φ, it is difficult to define a crystal plane which is exactly parallel with the sample surface. Therefore, the (012) planes

can be characterized to investigate the out-of-plane strain in (YXl)36° LN. In addition, the HRXRD measurements can
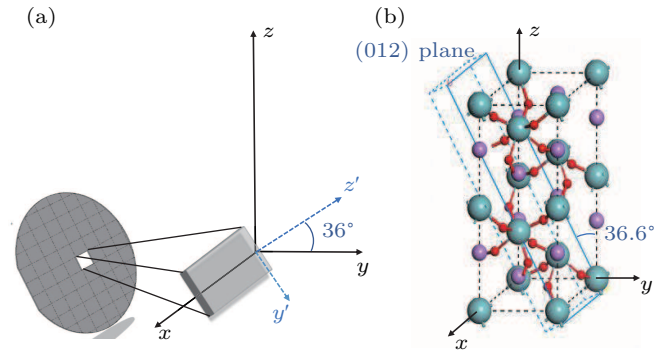

Fig. 1. (a) An illustration of the relationship between the coordinate system of the material crystal and the substrate structure for (YXl)36° cut LN. The angle between the sample surface and the z axis of LN crystal is 36°. (b) The atomic arrangement in the hexagonal unit cell of LN. The angle between the (012) plane and the z axis is about 36.6°.
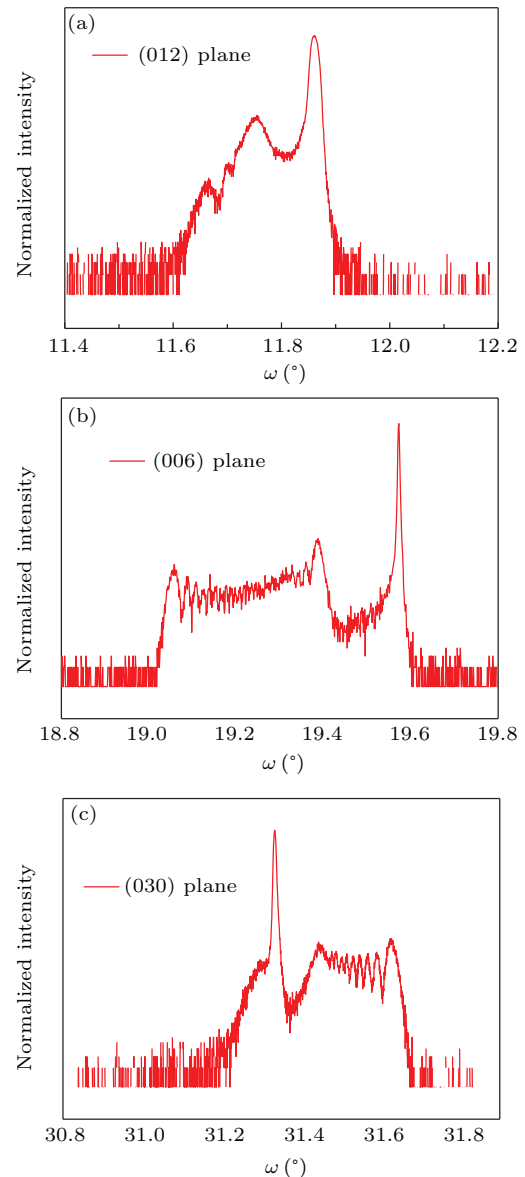

Fig. 2. The XRD coupled ω–2θ spectra of the (012) plane (a), the (006) plane (b), and the (030) plane (c) for He-implanted (YXl)36° cut LN samples.

be executed on the (030) and (006) planes by tilting the samples with certain offset angles. The ω–2θ XRD spectra of the He-implanted (YXl)36° LN are plotted in Fig. 2. The fringe patterns arise from the interferences between scattered beams induced by the damaged part of the crystal, and the fringe spacing is related to the width of the strained region for a given strain level.[29,30] The implantation-induced strain can be calculated according to the Bragg's theorem $\varepsilon_{max} = (\sin(\theta) - \sin(\theta + \Delta\theta))/\sin(\theta + \Delta\theta)$, where θ is the position of the main Brag diffraction peak and θ is the distance between the last peak and the main Bragg peak in angle. As shown in Fig. 2(a), the interference fringes of the XRD spectrum on the (012) plane extends from the left side of the main diffraction peak, indicating that the interstitial He induces out-of-plane tensile strain.[20,21,31] The relative lattice strain $\varepsilon_{(012)}$ is calculated to be about 1.618% by extracting the distance between the (012) Bragg diffraction peak and the farthest interference fringe. Meanwhile, a set of satellite peaks appear at the left side of the (006) LN main diffraction peak as shown in Fig. 2(b), and the relative lattice strain $\varepsilon_{(006)}$ deduced from the Bragg's theorem is 2.577%. However, the XRD spectrum on the (030) plane in Fig. 2(c) displays an intriguing strain profile. The main Brag peak is broadened at the left side while a series of satellite peaks exhibit at the right side. It is explicitly that the He ion implantation induces non-uniform strain in the (030) plane and the compressive strain dominates the strain profile. The out-of-plane strain of the (030) plane $\varepsilon_{(030)}$ is calculated to be -0.837%, in which the minus represents the lattice contraction of the implanted region compared with the undisturbed deeper region.

In addition to the strain gradient of irradiated layer which is characterized along the direction normal to the desired crystallographic plane, a complete description of the strain state of the implanted layer is presented. Figure 3(a) shows the XRD intensity of the symmetric RSM scanning on the (012) plane of the implanted (YXl)36° LN. The positions are located by the in-plane (q_x) and out-of-plane (q_z) components of the scattering vector, and the intensity is in logarithmic scale. The insert grey solid line represents the coupled ω–2θ scan of (012) plane. The strong signal (dashed part of the intensity map) corresponds to the main Bragg diffraction of Fig. 3(a) which represents the unirradiated part of the crystal. The spreading of the intensity in the region of higher lattice parameter emerges from the scattering by the damaged layer. Since the $2\theta_{(hkl)}/2 - \psi$ (ψ represents the angle between the (hkl) plane and the surface) of (030) and (006) planes are less than zero for the (YXl)36° cut LN samples, an asymmetric RSM around the (113) diffraction was recorded using the same ion implanted sample. As shown in Fig. 3(b), the two arrows, which share the same starting point located at the maximum intensity corresponding to the undisturbed part of the (YXl)36° cut LN, indicate the values of the in-plane (about 2.385 nm^{-1}) and out-

of-plane (about 5.082 nm^{-1}) scattering vector components in the substrate. The intensity spreading of the RSM derives from the diffraction caused by the damaged layer. It is noteworthy that the intensity distributions of the symmetric and asymmetric RSM are confined in a sharp q_x region, which indicates that there is no difference between the damaged layer and the substrate. In another words, no deformation occurs in the planes perpendicular to the surface (at least at this low damage level). On the contrary, the wide spread of the intensity along the q_z direction suggests a tensile normal strain in the damaged layer.
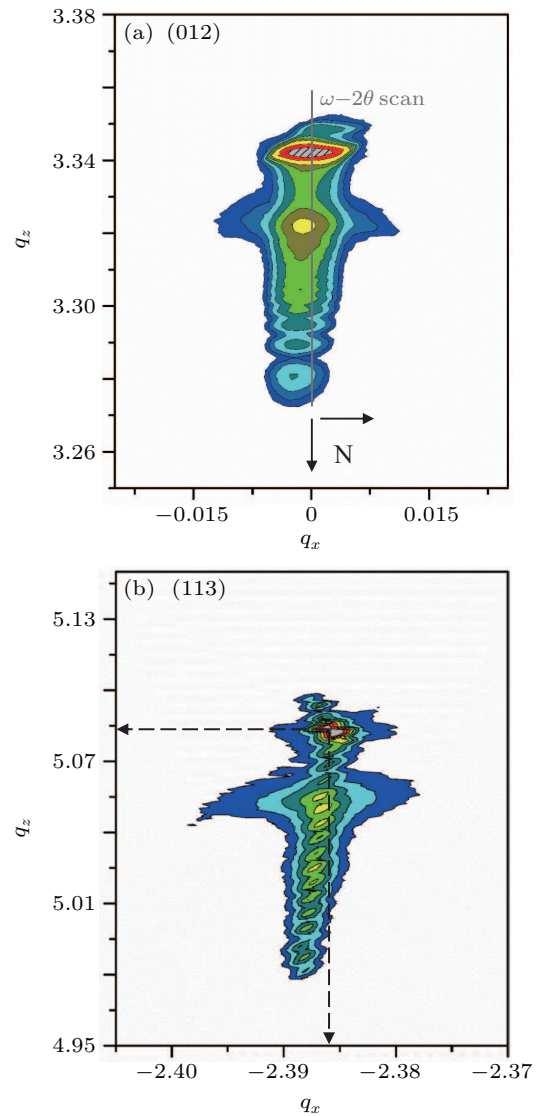

Fig. 3. Reciprocal space maps in the vicinity of the (012) Bragg diffraction (a) and the (113) Bragg diffraction (b) of the He-implanted (YXl)36° cut LN. The positions are located by the in-plane (q_x) and out-of-plane (q_z) components of scattering vector while the intensity is in logarithmic scale. The grey solid line displayed in panel (a) represents a coupled ω–2θ scan. The two arrows in panel (b) represent the values of the in-plane and out-of-plane scattering vector components in the unirradiated part of the crystal.

The schematic diagram of ion implanted (YXl)36° cut LN is shown in Fig. 4. For simplification, only the Nb atoms are plotted in the LN crystal structure. The red balls represent the implanted interstitial He ions. Similar with abundant reports of ion implanted Si,[32] He implantation induces

out-of-plane tensile strain along (012) plane. However, the insert the interstitial He ions rearranged due to the strong anisotropy of LN.[33,34] Different from the ion implantation which is widely used in the CIS of Si or SiC, the ion implantation induced strains in LN appear a distinct gap between main Bragg diffraction peak and the nearby interference fringe, it assumed to be a highly damaged or even amorphous layer which is similar to the ion implanted KTiOPO$_4$.[35] Therefore, it is distinguishing from the in-plane state of Si or SiC which is locked to the thick substrate. The redistribution of implanted He ions modified the strain profile and induced a large tension strain normal to the (006) plane. The measured lattice expansion $\varepsilon_{(006)}$ is approximately equal to the calculated value of 2.670%, which is deduced from the equation of $\varepsilon'_{(006)} = \varepsilon_{(012)}/\sin(36.6°)$. From the geometric point of view, the $\varepsilon_{(012)}$ can be regarded as one component of the $\varepsilon_{(006)}$. Meanwhile, the lattice contraction occurred in the (030) plane induces compressive strain. The $\varepsilon'_{(006)}$ is calculated to be -0.786% according to the equation of $\varepsilon'_{(030)} = -\nu_{zy}\varepsilon_{(006)}$, in which $\nu_{zy} = 0.29$ refers to the Poisson coefficient of LN for tracks along the z and y crystal axes.[34] The measured and calculated strain values are compared in Table 1, and the error between the calculation and the measurement is quite small for both the (006) and (030) plane. Therefore, the intriguing strain profile is inferred to be dominated by the ion redistribution. The redistributed He ions induce tensile strain normal to the (006) plane and then lead to the contraction of (030) planes, while some interstitial He ions disturb the strain profile mainly in the left side. In addition, the effect of the He fluence on the strain profile is investigated. The XRD coupled ω–2θ spectra on (030) plane of (YXl)36° cut LN implanted with various He fluence are plotted in Fig. 5. With the increase of the He fluence, the compressive strain increases from -0.811% to -0.895%, while the broaden at the left side of the peak diminished gradually. It indicates that the effect of interstitial ions is clear at low strain level while the ion redistribution plays a more important role with increasing the strain level.

Table 1. The measured and calculated strain values of different crystallographic planes in LN.

	Crystalline plane	Measured ε (%)	Calculated ε' (%)
	(012)	1.592	–
(YXl)36° LN	(030)	-0.837	-0.786
	(006)	2.577	2.670

In addition, the similar strain profile is observed in H-implanted (YXl)42° cut LT, and the coupled ω–2θ spectra are shown in Fig. 6. The intriguing strain profile is more obvious for the (YXl)42° cut LT. Two satellite peaks are observed on both sides of the main peak while the fringe patterns appear at the right side. That can be owing to the implanted induced strain level of H ions in LT is smaller than that of the one of He ions in LN. The redistributed H ions induce tensile

strain normal to the (006) plane and then lead to the contraction of (030) planes, while some interstitial H ions in different depth disturb the strain profile mainly in the left side. The ion-induced lattice expansion normal to the (006) plane and (012) plane is 1.213% and 0.655%, respectively. Meanwhile, the lattice contraction of (030) plane is about -0.295%. Similarly, the $\varepsilon'_{(006)}$ is calculated to be 1.094% deduced from $\varepsilon_{(012)}$ divide by $\sin(36.7°)$, and the $\varepsilon'_{(030)}$ is calculated to be -0.303% via $-\nu_{zy}\varepsilon_{(006)}$, in which 36.7° is the angle between (012) and (006) planes and the ν_{zy} of 0.25 refers to the Poisson coefficient of LT. The measured and calculated strains are shown in Table 2. In addition, the lattice contraction phenomenon is also observed in the highly anisotropic KTiOPO$_4$ implanted with H and He ions.[35]
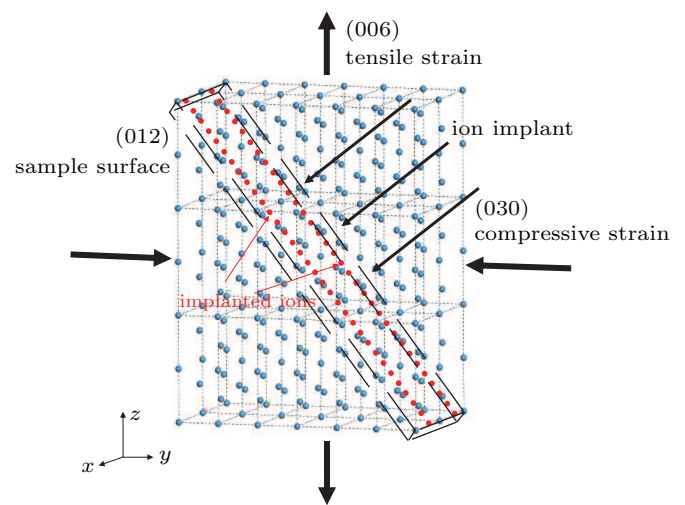

Fig. 4. The corresponding crystalline schematic diagram of the strains in implanted (YXl)36° cut LN. To facilitate the presentation of the structure, only the biggest Nb atoms are shown in this diagram, and the red balls represent the implanted He ions.
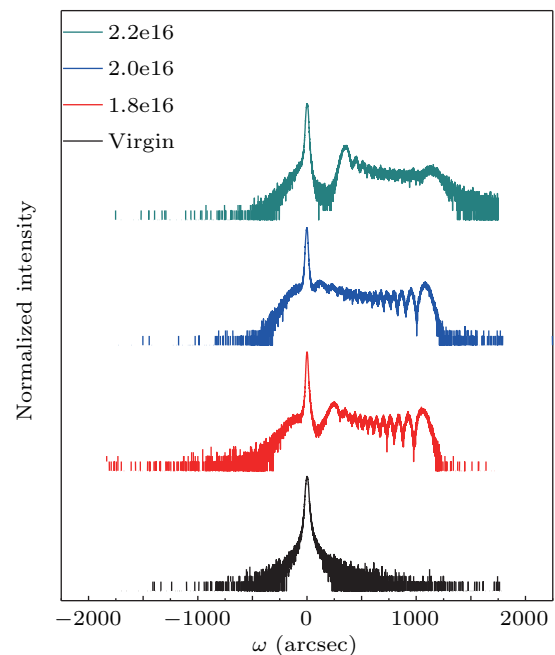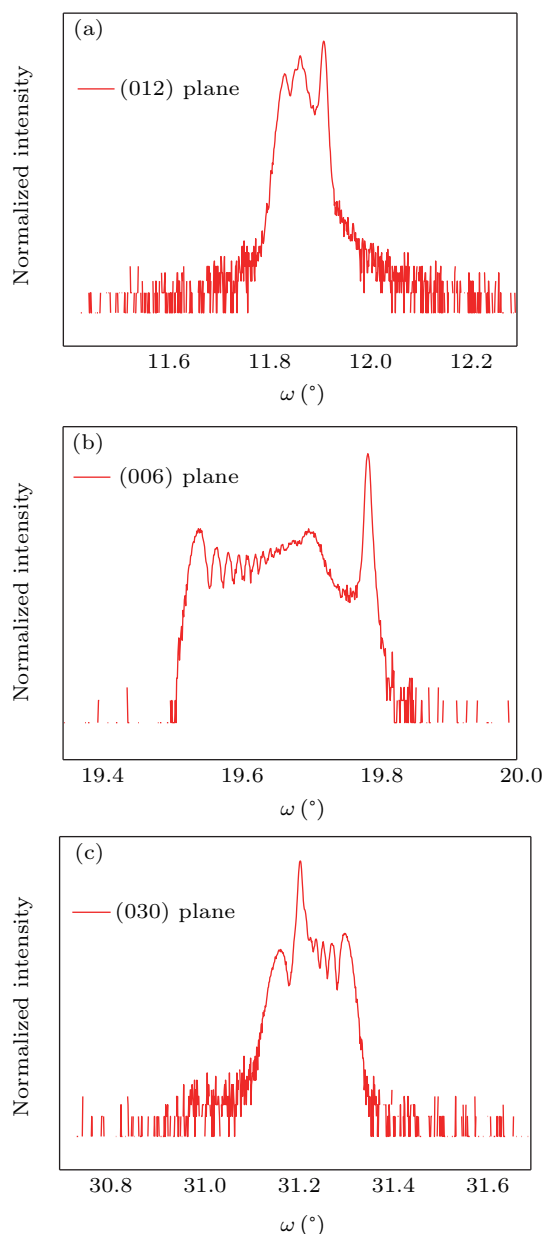

Fig. 5. The XRD coupled ω–2θ scan of (030) plane of implanted He ions in (YXl)36° cut LN with different fluence.

Table 2. The measured and calculated strain values of different crystallographic planes in LT.

	Measured plane	Measured (%)	Calculated (%)
(YXl)42° LT	(012)	0.655	–
	(030)	−0.295	−0.303
	(006)	1.213	1.094

Fig. 6. The XRD coupled ω–2θ spectra of the (012) plane (a), the (006) plane (b), and the (030) plane (c) for H-implanted (YXl)42° cut LT samples.

4. Summary

The understanding of implantation-induced strain is of vital importance to transfer single-crystalline piezoelectric film with various orientations. Here, we investigated the strain profile in the implanted rotated Y-cut LN and LT with ω–2θ scan and RSM. As the (012) plane is nearly parallel with the surface, the out-of-plane strain is calculated using the XRD spectra measured on the (012) plane. The ion implantation induced tensile strain of the (012) and (006) planes, while the strain of the (006) plane was bigger than that of the (012) plane due to the ion redistribution. From the geometry point of view, the tensile strain of the (012) plane can be regarded as one component of the strain of the (006) plane. Meanwhile, the lattice expansion of the (006) plane induces compressive strain of the (030) plane due to the Poisson effect, while the interstitial ions disturbs the strain profile. This work opens avenues to further understand the ion implantation induced strain in LN and LT for the preparation of POI substrate that seems to best satisfy the requirements for high performance SAW filters in mobile applications.

References

[1] Afif O, Federico B, Volker B, Katsutoshi K, Patrick M, Michal M, Olav Q, Malte S, Hans S, Hidekazu T, Hugo T, Mikko A U, Bogdan T and F M 2014 *IEEE Commun. Mag.* 26
[2] Wang C X, Haider F, Gao X Q, You X H, Yang Y, Yuan D F, Aggoune H M, Haas H, Fletcher S and Hepsaydir E 2014 *IEEE Commun. Mag.* **52** 122
[3] Arun A, M G and A K 2015 *J. Electr. Electron. Eng. Ame.* **3** 22
[4] Gupta A and Jha R K 2015 *IEEE Access* **3** 1206
[5] Schulz M B, Matsinger B J and Holland M G 1970 *J. Appl. Phys.* **41** 2755
[6] Neurgaonkar R R, Kalisher M H, Lim T C, Staples E J and Keester K L 1980 *Mater. Res. Bull.* **15** 1235
[7] Ruby R 2015 *IEEE Microw. Mag.* **16** 46
[8] Gorisse M, Drouin A, Sinquin Y, Huyet I, Courjon E, Bernard F, Clairet A, Laroche T, Bousquet M, Reinhardt A, Butaud E, Ballandras S and Radu I 2018 *IEEE International Ultrasonics Symposium*, October 22–25, Kobe, Japan
[9] Bhugra H and Piazza G 2017 *Piezoelectric MEMS Resonators* (Springer International Publishing, Cham, Switzerland), p. 99
[10] Plessky V, Yandrapalli S, Turner P J, Villanueva L G, Koskela J and Hammond R B 2019 *Electron. Lett.* **55** 98
[11] Takai T, Iwamoto H, Takamine Y, Fuyutsume T, Nakao T, Hiramoto M, Toi T and Koshino M 2017 *IEEE International Ultrasonics Symposium*, September 6–9, 2017, Washington, DC, USA
[12] Emad A, Lu R, Li M H, Yang Y, Wu T and Gong S 2019 *IEEE 32nd International Conference on Micro Electro Mechanical Systems*, Januaray 27–31, 2019, Seoul, South Korea, 282
[13] Gruber M, Konetschnik R, Popov M, Spitaler J, Supancic P, Kiener D and Bermejo R 2018 *Acta Mater.* **150** 373
[14] Nishimura E, Okano K, Terashima A and Hoshikawa K 2019 *Cryst. Res. Technol.* **54** 1900023
[15] Reinhardt A, Benaissa L, David J B, Lamard N, Kovacova V, Boudou N and Defas E 2014 *IEEE International Ultrasonics Symposium*, September 3–6, 2014, Chicago, IL, USA, 773
[16] Sun W W, Zheng X F, Fan S, Wang C, Du M, Zhang K, Chen W W, Cao Y R, Mao W, Ma X H, Zhang J C and Hao Y 2015 *Chin. Phys. B* **24** 017303
[17] Liao Q, Li B, Kang L and Li X 2020 *Chin. Phys. B* **29** 076103
[18] Yan Y, Huang K, Zhou H, Zhao X, Li W, Li Z, Yi A, Huang H, Lin J, Zhang S, Zhou M, Xie J, Zeng X, Liu R, Yu W, You T and Ou X 2019 *ACS Appl. Electron. Mater.* **1** 1660
[19] Moram M A and Vickers M E 2009 *Rep. Prog. Phys.* **72** 036502
[20] Huang K, Li Z, Yan Y, Zhao X, Li W, You T, Zhang S, Zhou H, Lin J, Xu W, Yi A, Huang H, Zhou M, Yu W, Xie J, Zeng X, Liu R and Ou X 2019 *AIP Adv.* **9** 085001

[21] Bianconi M, Argiolas N, Bazzan M, Bentini G G, Cerutti A, Chiarini M, Pennestri G, Mazzoldi P and Sada C 2007 *Nucl. Instrum. Methods Phys. Res. Sect. B-Beam Interact. Mater. Atoms* **249** 122

[22] Ma C, Lu F and Ma Y 2015 *Nucl. Instrum. Methods Phys. Res. Sect. B-Beam Interact. Mater. Atoms* **342** 76

[23] Stoller R E, Toloczko M B, Was G S, Certain A G, Dwaraknath S and Garner F A 2013 *Nucl. Instrum. Methods Phys. Res. Sect. B-Beam Interact. Mater. Atoms* **310** 75

[24] Morgan D 2007 *Surface Acoustic Wave Filters* (Northampton: Academic Press) p. 91

[25] Shibayama K, Yamanouchi K, Sato H and Meguro T 1976 *Proc. IEEE* **64** 595

[26] Weis R S and Gaylord T K 1985 *Appl. Phys. A* **37** 191

[27] Hsu R, Maslen E N, Duboulay D and Ishizawa N 1997 *Acta Crystallogr. Sect. B-Struct. Commun.* **53** 420

[28] Wong K K 2002 *Properties of Lithium Niobate* (INSPEC, The Institution of Electrical Engineers, London, United Kingdom) p. 9

[29] Ghatak J, Satpati B, Umananda M, Satyam P V, Akimoto K, Ito K and Emoto T 2006 *Nucl. Instrum. Methods Phys. Res. Sect. B-Beam Interact. Mater. Atoms* **244** 64

[30] Sousbie N, Capello L, Eymery J and Rieutord F 2006 *J. Appl. Phys.* **99** 103509

[31] Debelle A and Declémy A 2010 *Nucl. Instrum. Methods Phys. Res. Sect. B-Beam Interact. Mater. Atoms* **268** 1460

[32] Benton J L, Libertino S, Kringho J P, Eaglesham D J, Poate J M and Coffa S 1997 *J. Appl. Phys.* **82** 120

[33] Gotz G and Karge H 1983 *Nucl. Instrum. Methods Phys. Res.* **209** 1079

[34] Rivera A, Garcia G, Olivares J, Crespillo M L and Agulló-López F 2011 *J. Phys. D: Appl. Phys.* **44** 475301

[35] Ma C, Lu F, Li K and Liu K 2018 *Mater. Res. Express* **5** 025204